Received 28 April 2024; accepted 19 May 2024. Date of publication 27 May 2024; date of current version 6 August 2024.

Digital Object Identifier 10.1109/OJAP.2024.3405849

Design Guidelines and Performance Analysis of a Wideband Coaxial Horn Antenna Fabricated via Additive Manufacturing

ELÍGIA SIMIONATO[1] (Student Member, IEEE), IVAN ALDAYA[1] (Member, IEEE), JOSÉ A. DE OLIVEIRA[1], ANDRE L. JARDINI[2], JULIAN AVILA[1], GUILHERME S. DA ROSA[1] (Senior Member, IEEE), AND RAFAEL A. PENCHEL[1] (Member, IEEE)

[1]School of Engineering, São Paulo State University, São João da Boa Vista 13876-750, Brazil

[2]National Institute of Science and Technology in Biomanufacturing, Faculty of Chemical Engineering, University of Campinas, Campinas 13083-970, Brazil

CORRESPONDING AUTHOR: R. A. PENCHEL (e-mail: rafael.penchel@unesp.br)

This work was supported in part by the Brazilian Agencies National Council for Scientific and Technological Development (CNPq) under Grant 409146/2021-8; in part by the São Paulo Research Foundation (FAPESP) under Grant 2019/20209-8 and Grant 2020/09889-4; and in part by the Brazilian Agency FINEP under Grant 0527/18.

ABSTRACT This work introduces a Ka-band coaxial horn antenna that incorporates a specialized dielectric supporting structure and a transition to a 2.4 mm connector. The inner and outer radii of the coaxial aperture were sized using an approximated model for an open-ended coaxial waveguide. The theory of small reflections was then used to account for the reflection coefficient resulting from an additional cascading cylindrical-conical section. A refined numerical model, representing more accurately a prototype, featured a transition region to standardized connectors and a dielectric structure that offers mechanical support for the inner conductor and impedance matching. Ansys HFSS full-wave electromagnetic finite-element method solver was used to compute the parameters of the antenna, and a genetic algorithm optimizer was employed to improve the performance of the complete coaxial horn. A prototype was fabricated using metal additive manufacturing for the inner and outer horn conductors, while the dielectric support was created using 3D polymer printing. Experimental measurements demonstrate that the prototyped antenna has an impedance bandwidth of above 79.36% (19–44 GHz), a peak realized gain of 11.53 dBi, and a maximum efficiency of 89.83%. Additionally, a sensitivity analysis was conducted to evaluate the potential impact of additive manufacturing imperfections and assembly errors on the antenna's performance.

INDEX TERMS Wideband antenna, dual-reflector antenna, coaxial horn, conical-beam radiation, coaxial waveguide, additive manufacturing, Ka-band, millimeter-wave.

I. INTRODUCTION

TO MEET the increasing demand for high-quality wireless communication, the millimeter-wave (mm-wave) band has garnered significant attention as a promising choice for 5G, 6G, and other future wireless technologies. Such communication systems face challenges such as elevated atmospheric propagation loss and limited performance in non-line-of-sight conditions. Integrating mm-wave communication systems with lower frequency bands is anticipated to overcome these limitations. Sub-6 GHz bands are employed for wider coverage and better penetration, while the mm-wave Ka-band is leveraged for higher data transfer rates and capacity. In this context, base stations play a crucial role in mm-wave communication systems, where omnidirectional antennas are well-suited due to their ability to provide full 360-degree coverage for point-to-multipoint applications.

At mm-wave frequencies, high-gain broadband antennas (above 10 dBi for an omnidirectional pattern) are required in many wireless applications to compensate for free-space path loss, atmospheric absorption, and limited transmit

power [1], [2]. A collinear antenna array of electrical or magnetic dipoles can accomplish this with a narrow impedance bandwidth. The traveling-wave antennas such as discone and biconical can produce a wider bandwidth, although their typical peak gain varies from 1 to 7 dBi [3], [4]. Traveling-wave arrays using elements such as biconical antennas and slotted waveguides are suitable to attain high gain with impedance bandwidth larger than 20%, although they do not offer steady-frequency vertical radiation pattern due to the inherent frequency-beam-steering behavior [4], [5], [6].

Recently, several research efforts have been dedicated to the design and development of non-planar wideband high-gain omnidirectional antennas with frequency-stable vertical radiation pattern operating in the Ka-band [3], [6], [7], [8], [9], [10], [11], [12], [13]. In [3], two biconical antenna elements are arranged and differentially fed, exhibiting an impedance bandwidth (with reflection coefficient better than −10 dB) of 14.2%, over 26.2 GHz to 30.2 GHz, and with a maximum gain of 12.5 dBi. In [6], a complex antenna system composed of a biconical antenna loaded with an annular metal lens and its dielectric holding was designed for the Ka-band. The antenna exhibited an −10 dB impedance and 3 dB gain bandwidths of 43.9% (25.6 GHz–40.0 GHz). The maximum measured gain achieved was 9.2 dBi. The main limitation of this model is associated with the manufacturing and assembly of the metal lens and their supports, which can make the model more vulnerable to imperfections. In the study in [7], an annular slot technique was employed to enhance the impedance performance of a monopole antenna while maintaining consistent radiation patterns. The antenna achieved a voltage standing wave ratio below 2 from 17.9 to 50 GHz, with a flat gain of approximately 5.5 dBi.

The omnidirectional dual-reflector antenna fed by a TEM coaxial horn is a high-efficiency option suitable to operate in mm-wave frequencies [9], [10]. It offers the advantage of providing omnidirectional high gain with a wideband behavior with a steady-frequency vertical radiation pattern. The simulations results in [10] reveal that the geometric optics (GO)-shaped reflector shows a frequency bandwidth larger than 45% (25–40 GHz) for $|S_{11}| \leq -20$ dB with a maximum directivity of approximately 14 dBi. The gain of these antennas is directly linked to the electrical size of the antenna aperture. The bandwidth, on the other hand, is primarily influenced by the characteristics of the feeder, typically a conical-beam radiation antenna with a null at the axial direction (z-positive) to avoid reflection at the feeder.

The design and fabrication of an operational coaxial horn operating at the X band, similar to that presented in [10], were analyzed in [12], showing a 30% relative bandwidth. This approach uses a transition to an N-type connector, and a dielectric support structure for the inner conductor was presented. However, implementing the proposed dielectric structure requires a complex manufacturing process, in which the horn needs to be constructed in several separate parts assembled after the dielectric is inserted. Another drawback of this approach is that manufacturing errors severely degrade the reflection coefficient. A similar design projected for the Ka-band was presented in [10]. However, it does not consider a supporting structure for the inner conductor or an appropriate coupler for standardized connectors. These issues were investigated numerically in [13], but the results were not validated experimentally. In addition to lacking measured results and experimental validation, the work in [13] does not present design guidelines and does not give details about the reported supporting structure or the coupling to standardized connectors. Also, the presented design considers coupling to a 2.92 mm connector, which may limit the coaxial horn operation up to 40 GHz.

An alternative coaxial feeder design was recently reported in [11], where the authors analyzed a circular aperture horn antenna with a conical radiation pattern radiating the fundamental transverse magnetic field (TM_{01} mode). The antenna consists of a coaxial waveguide and a quadruple-ridged conical horn fabricated using laser-based powder bed fusion (L-PBF). Experimental measurements show that a wide relative impedance bandwidth of 60.7% and a peak gain of 11.4 dBi can be achieved within the frequency band ranging from 24.9 to 46.6 GHz. Considering the miniaturization of devices, the radiation of the TM_{01} mode poses a limitation due to its dependence on efficient coaxial to circular transmission. Additionally, the operation of this mode is only feasible above the cutoff frequency for such a mode. On the other hand, coaxial horns offer distinct advantages, particularly in terms of not having a cutoff frequency for the TEM mode, and also facilitate the conversion of the field to TM modes with wide-band characteristics [10], [12]. Furthermore, when compared to the antenna in [11], the TEM horn, with its inner conductor, provides an additional degree of freedom for controlling the field distribution. This characteristic not only enhances the capacity to shape the field distribution precisely but also enables easy integration with reflector antennas.

In this article, we explore the design of a coaxial horn antenna to address the aforementioned theoretical and practical gaps in the literature. Firstly, we introduce working principles, design guidelines equations, and an approximate analytical model for the coaxial horn. A novel ogival-like dielectric support for the inner conductor was proposed, as well as the transition to a 2.4 mm connector [14]. The performance of the horn antenna was assessed through rigorous analysis employing the finite element method in Ansys HFSS. To improve the antenna's performance, a multi-objective genetic algorithm (GA) was utilized to optimize the dimensions of both the dielectric structure and the transition section.

A prototype of the antenna was fabricated using additive manufacturing (AM), specifically, L-PBF for the metallic inner and outer conductors, and polymeric printing for the dielectric support. The rest of this work is organized as follows. Section II presents the geometry of the coaxial antenna and procedures for its design. Initially, Section II

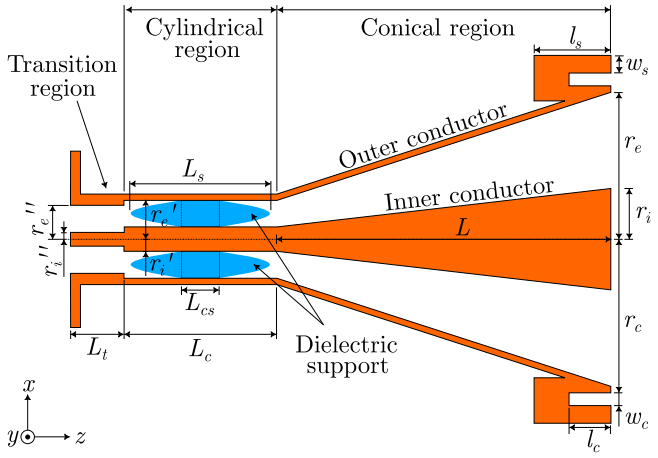

FIGURE 1. Geometry of the coaxial horn antenna.

describes the coaxial horn using approximate models for an open-ended coaxial waveguide (Section II-B) and cascaded cylindrical-conical coaxial sections (Section II-C). Then, a refined model representing a functional prototype is discussed and optimized in Section II-D. Section III describes the fabrication via AM and presents numerical and experimental results. In addition, a sensitivity analysis of imperfections in antenna fabrication and assembly and their consequences for impedance matching and radiation characteristics is presented. Finally, concluding remarks are presented in Section IV.

II. COAXIAL HORN DESIGN

The proposed design for the coaxial horn comprises three main parts, as depicted in Fig. 1: a) a transition region that serves to change the radii of the conductors from a standard 2.4 mm connector, b) a cylindrical region containing a dielectric support structure, and c) a conical region extending to the aperture of the horn. A corrugation is introduced at the aperture edge to minimize the backscattering radiation [12]. The horn used in this study was based on the one described in [10], with the inclusion of a transition region and a dielectric structure designed to provide mechanical support to the inner conductor and ensure impedance matching.

A. WORKING PRINCIPLES AND DESIGN GUIDELINES

The basic principles of operation of a coaxial horn are well known [15]. Briefly, the modal TEM fields in a coaxial waveguide are radiated into free space. The gain of this horn increases with the external radius r_e, but the excitation of higher-order modes should be avoided for practical applications. Thus, optimized performance requires that the inner radius r_i grows along with r_e so that only the fundamental mode propagates. In view of that, the design of an antenna incorporating a coaxial aperture necessitates the implementation of a conical interface between the aperture and a standardized coaxial connector. This design criterion is pivotal to ensure that the TEM field is transmitted primarily along the axial direction of the antenna. Such a transition is effectively facilitated by the antenna's design, which includes distinct conical and cylindrical sections. This configuration is detailed in Fig. 1, illustrating the critical transition zones that enable the desired propagation characteristics.

B. APPROXIMATED MODEL FOR AN OPEN-ENDED COAXIAL WAVEGUIDE

Our design process started with sizing the antenna aperture radii to maximize directivity and minimize reflection from a coaxial aperture radiating into free space. At this stage, the effects of the cylindrical and conical regions were neglected. Assuming that the dimensions of the radii of the inner and outer conductors of the coaxial aperture allow only the propagation of the TEM mode, the normalized electromagnetic fields in a planar aperture in a coaxial waveguide, expressed in cylindrical coordinates (ρ, ϕ, z), are defined by

$$E_\rho = \frac{1}{\rho}, \quad \text{and} \quad H_\phi = \frac{1}{\eta\rho}, \tag{1}$$

with all other field components being null. In the above, η represents the wave impedance of the TEM mode.

We can approximate the radiated fields of the above coaxial waveguide into semi-infinite space through the Kirchhoff-Huygens principle, also known as the aperture-field method, as discussed in [16, Ch. 10], [2, Ch. 12]. Accordingly, the pertinent electric far-field components in spherical coordinates (r, θ, ϕ) are given by

$$E_\theta = \frac{e^{-jkr}}{r}\frac{1}{2\sin\theta}\left[1+\cos\theta+\Gamma_{\text{ap}}(1-\cos\theta)\right] \times[J_0(kr_e\sin\theta) - J_0(kr_i\sin\theta)], \tag{2}$$

$$E_\phi = 0, \tag{3}$$

where k denotes the working wavenumber, and $J_0(\cdot)$ is a Bessel function of the first kind and order zero. The method described in [16, Ch. 10] has been employed here to account for the aperture reflection from the open-ended waveguide, albeit adapted for a coaxial aperture scenario. It is important to note that as $\Gamma_{\text{ap}} \to 0$, the formulas presented revert to those utilized in [17]. As a consequence of the circular symmetry of the aperture fields as indicated in (1), the associated radiated fields are also symmetric with respect to ϕ, resulting in the absence of cross-polarized fields.

An approximation for the reflection coefficient can be computed via

$$\Gamma_{\text{ap}} = \frac{y_{\text{ap}} - 1}{y_{\text{ap}} + 1} \tag{4}$$

where y_{ap} is the equivalent aperture admittance normalized by the characteristic admittance of the TEM mode of the coaxial waveguide. Variational approximated formulas for calculating y_{ap} are available in [18, Sec. 4-16], enabling its computation as follows:

$$y_{\text{ap}} = g_{\text{ap}} + jb_{\text{ap}} \tag{5}$$

with

$$g_{\text{ap}} = \frac{1}{\log\left(\dfrac{r_e}{r_i}\right)} \int_{\vartheta=0}^{\pi/2} \frac{[J_0(kr_e \sin\vartheta) - J_0(kr_i \sin\vartheta)]^2}{\sin\vartheta}\, d\vartheta \tag{6}$$

$$b_{\text{ap}} = \frac{1}{\pi \log\left(\dfrac{r_e}{r_i}\right)} \int_{\vartheta=0}^{\pi} 2\,\text{Si}\left(k\left(r_e^2 + r_i^2 - 2r_e r_i \cos\vartheta\right)^{1/2}\right) - \text{Si}(2kr_e \sin(\vartheta/2)) - \text{Si}(2kr_i \sin(\vartheta/2))\, d\vartheta \tag{7}$$

where $\text{Si}(\cdot)$ is the sine integral function.

The formulas approximated above were used to obtain a first estimation of the ideal horn aperture dimensions in terms of radiation and impedance matching characteristics, with the directivity being approximated via [2, eq. (2-16)]

$$D_{\text{ap}} = 4\pi \frac{U_{\text{ap, max}}}{P_{\text{ap, rad}}} \tag{8}$$

where the maximum radiation intensity is easily computed via

$$U_{\text{ap, max}} = |E_{\theta,\,\text{max}}|^2 \tag{9}$$

and the radiated power obtained via the numerical evaluation of the integral

$$P_{\text{ap, rad}} = 2\pi \int_{\theta=0}^{\pi} |E_\theta|^2 \sin\theta\, d\theta. \tag{10}$$

In the above, $E_{\theta,\,\text{max}}$ represents the field computed via (2) (for a fixed r) in the direction of maximum radiation.

Assuming an external aperture radius $r_e = 10.28$ mm, we analyze the effect of the ratio r_e/r_i of the aperture on the results shown in Fig. 2. Besides minimal changes being observed for the directivity over the frequency range of interest, the correct choice of an inner aperture radius allows us to minimize the reflection. Since a high r_e/r_i ratio is not ideal due to construction constraints, we observe in Fig. 2 that a ratio between 2.5 and 3 leads to a good balance between impedance bandwidth and maximum directivity over the Ka-band.

Again, it is crucial to note that the approximated model does not encompass the scattering associated with other internal regions (such as transition, cylindrical, and conical regions), nor does it consider the effects of the outer geometry with flanges and external parts. Additional reflections beyond the aperture reflection, approximated via equation (4), need to be taken into consideration for precise modeling of the antenna's overall reflection mismatching looking to the 2.4 mm input connector. Concerning the external components, our design has incorporated a ring choke with a depth ℓ_c and width w_c to mitigate backradiation levels, as suggested in [19], thus making the approximated prediction in (2) representative, at least within the main radiation conical lobe. This choke will effectively reduce the impact of diffraction resulting from the finite-length antenna flange, rendering the corrections described in [20] unnecessary.

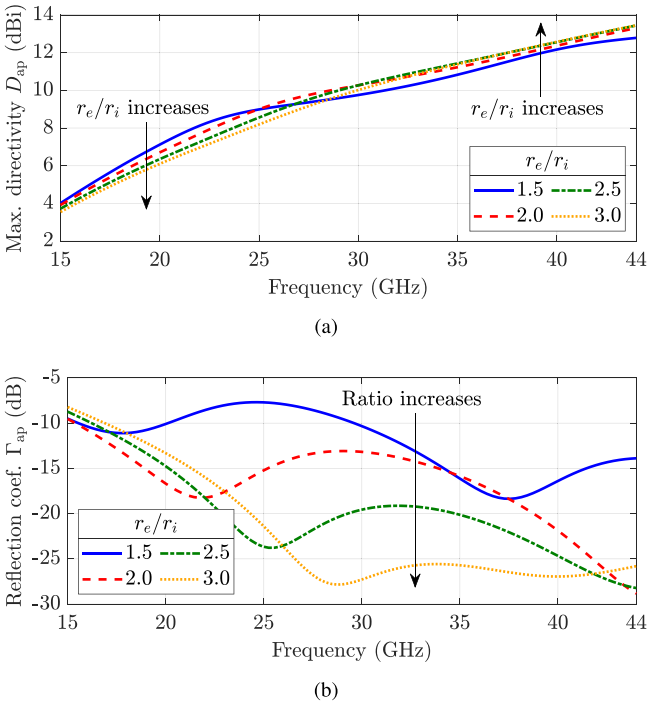

FIGURE 2. Simulated results of parametric analyses for aperture the ratio r_e/r_i. (a) Maximum antenna directivity $D_{\text{ap, max}}$. (b) Aperture reflection coefficient Γ_{ap}.

C. APPROXIMATED MODEL FOR CASCADED CYLINDRICAL-CONICAL COAXIAL SECTIONS

In the conical region, the coaxial domain has inner and outer radii that vary from r_i' and r_e' (at the connection of the cylindrical region) to r_i and r_e (at the antenna aperture) over a longitudinal span of length L, as depicted in Fig. 1. The reflection coefficient $\Gamma_{\text{cyl,con}}$ seen at the cylindrical to conical region interface can be treated as contributions from the aperture and the tapered section. Assuming continuously tapered inner and outer metallic conductors, as described in the theory of small reflections [21, Secs. 5.5–5.8], to the present context, we can approximate such reflection as

$$\Gamma_{\text{cyl,con}} = \frac{1}{2} \int_{z=0}^{L} e^{-j2kz} \frac{Z'_{\text{taper}}(z)}{Z_{\text{taper}}(z)}\, dz + \Gamma_{\text{ap}} \tag{11}$$

where the local coaxial impedance as a function of position is defined by

$$Z_{\text{taper}}(z) = \frac{\eta}{2\pi} \log\left[\frac{b(z)}{a(z)}\right] \tag{12}$$

and the taper is accounted for via the linearly varying radii

$$a(z) = r_i' + \frac{r_i - r_i'}{L} z, \tag{13}$$

$$b(z) = r_e' + \frac{r_e - r_e'}{L} z. \tag{14}$$

In (11), the derivative with respect to z of the local impedance, i.e., $Z'_{\text{taper}}(z)$, can be easily computed analytically from (12), but the integral must be performed numerically.

By using the aperture size defined with $r_i = 3.75$ mm and $r_e = 10.28$ mm, i.e., a ratio of 2.74, and assuming that

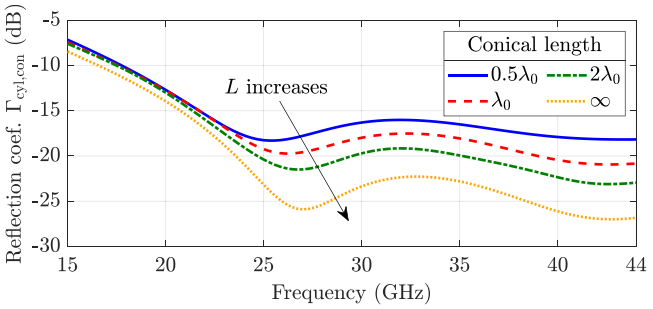

FIGURE 3. Simulated reflection coefficient $|\Gamma_{cyl,con}|$ as a function of the conical section length L.

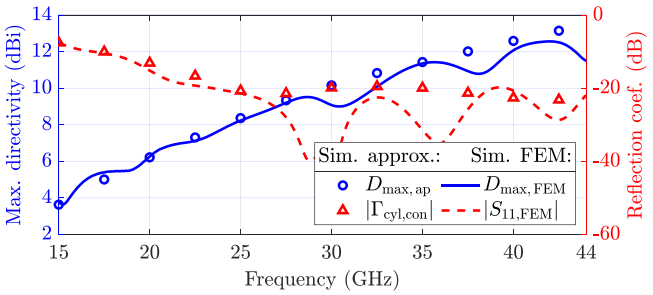

FIGURE 4. Maximum directivity and reflection coefficient of the horn antenna simulated using the approximate method and via FEM.

the coaxial waveguide at the beginning of the conical region has $r_i' = 0.83$ mm and $r_e' = 1.908$ mm, we have computed the approximate reflection coefficient depicted in Fig. 3 for conical lengths $L = \{0.5, 1, 2\}\lambda_0$, with $\lambda_0 = 10.714$ mm. In the limiting scenario as $L \to \infty$, we have $\Gamma_{cyl,con} \to \Gamma_{ap}$. It is observed that the reflection coefficient can be minimized to the level of that at the aperture using long lengths L, but this impacts the size of the horn. A good balance between size and performance is achieved with $L = 2.17\lambda_0$, proving a reflection coefficient of about -20 dB over the Ka-band. Fig. 4 shows the reflection coefficient and maximum directivity of the antenna simulated using the approximate method and FEM, demonstrating relatively good agreement at low frequencies where the horn supports single-mode propagation. The corresponding radiation patterns at relevant Ka-band frequencies 26 GHz, 33 GHz, and 40 GHz are depicted in Fig. 5. The approximated model accurately predicts the main radiation lobes; however, its precision decreases as the frequency increases due to the effects of higher-order modes that are not considered.

The proposed design differs from other designs documented in the literature, enabling a wideband characteristic. For instance, the length of the conical section used in [17] is approximately one-third of the central operating wavelength. Evaluations based on the results depicted in Fig. 2(b) suggest that a length L about twice the wavelength (or more) leads to a more favorable reflection characteristic. Additionally, unlike [17], the current design avoids a direct connection between a standard coaxial connector and the conical section. Typically, commercial coaxial connectors come with

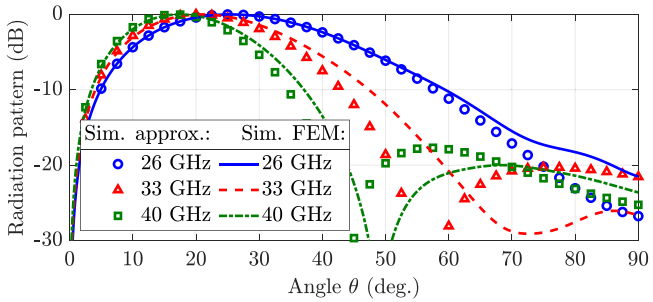

FIGURE 5. Normalized radiation patterns at 26 GHz, 33 GHz, and 40 GHz simulated via the approximated method and via FEM.

dielectric support, and their direct integration with an air-filled coaxial waveguide of the same cross-section may result in an additional impedance mismatch beyond that indicated by the approximations in (11). To address this, the proposed antenna design includes an extra transition region, as shown in Fig. 1. It is also important to note that dielectric support is essential for maintaining the spatial separation between the inner and outer conductors. The modeling of these elements in both the cylindrical and transition regions will be further detailed in the following section.

D. REFINED MODEL FOR COMPLETE COAXIAL HORN

In order to obtain a feasible prototype, two main modifications were made to the simplified model of the coaxial horn, presented in Section II-C: first, the addition of a dielectric support and matching structure in the cylindrical region (refer to Fig. 1), and second, the addition of a transition region. These modifications were first implemented, verified, and improved through parametric analysis utilizing the finite-element method (FEM) solver of ANSYS HFSS [22]. Metallic structures were considered as perfect electric conductors, and the dielectric support was implemented in PA2200 Polyamide 12 (Nylon 12) with loss tangent of $\tan\delta = 0.07$, and relative permittivity $\epsilon_r = 3.8$ [23]. The effect of roughness and the finite electrical conductivity of the metal-additive-manufacturing material were ignored.

Considering first the addition of a mechanical support to the inner conductor, we know that the introduction of a dielectric structure with $\epsilon_r > 1$ in a region previously filled by air alters the impedance, requiring a solution for matching. Reference [12] employed a cylindrical structure to achieve this by altering the cylindrical region radii and dimensioning the support structure to minimize reflections. However, this approach resulted in a geometry posing manufacturing difficulties, as detailed in Section I.

We tested several geometries with the aim of developing a new structure that needed to serve as both a mechanical support for the inner conductor and an impedance-matching element. Importantly, it should not negatively impact the performance of the coaxial horn and should also facilitate the manufacturing process. To achieve this, all geometries were designed to fit precisely in the space between the inner and outer conductor within the cylindrical region.

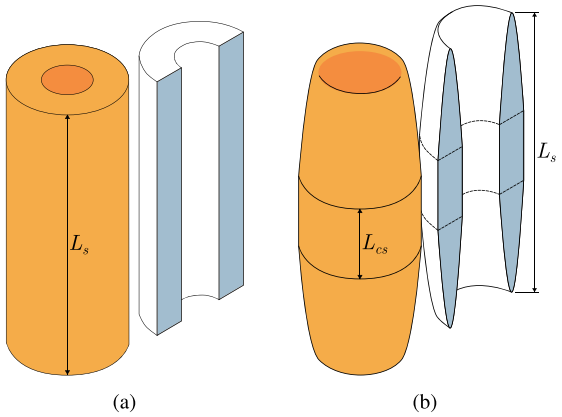

FIGURE 6. Examples of geometries considered in the development of the impedance matching structure.

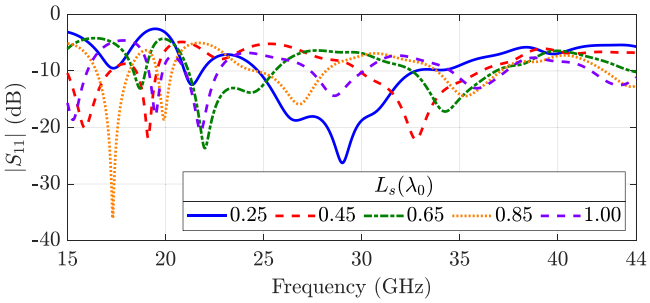

FIGURE 7. Reflection coefficients simulated via FEM for the analyzed variations in the length of the cylindrical support (Fig. 6(a)).

Initially, the same cylindrical geometry used in [12] was applied in this work, but without altering the radii corresponding to the inner and outer conductor. This geometry is depicted in Fig. 6(a). The dielectric cylinder was placed at the center of the cylindrical region, its length was initially set to $\lambda_0/4$, and subsequently, a parametric analysis was conducted considering its length. Given that modifications to the cylindrical region do not result in significant changes in the radiation pattern, we verified only the reflection coefficient. The reflection coefficients for the parametric analysis of the length of the cylindrical support are presented in Fig. 7. Generally, the use of the cylindrical support degraded the performance of the coaxial horn, leading to an increased reflection coefficient that remains between -20 dB and -5 dB for most of the analyzed frequency band.

Subsequently, the performance of the coaxial horn was assessed with the support designed to provide a soft transition from air to Polyamide 12 and back to air. This support design, illustrated in Fig. 6(b), comprised a cylindrical section and half-ogival end parts with equal lengths positioned at the beginning and end of the cylindrical section. The half-ogival parts can be described in Cartesian coordinates by:

$$X(t) = t \tag{15}$$

$$Y(t) = 0 \tag{16}$$

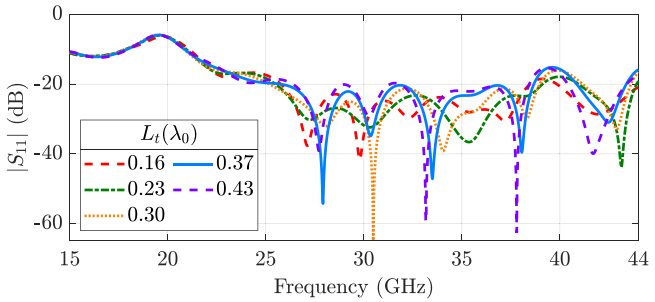

FIGURE 8. Reflection coefficients simulated via FEM for analyzed variations in the transition region's length (L_t).

$$Z(t) = \frac{L_s - L_{cs}}{2} - \frac{(L_s - L_{cs}) \cdot \left[2t - r'_e - r'_i)\right]^2}{2 \cdot \left(r'_e - r'_i\right)^2} \tag{17}$$

where $r'_i \leq t \leq r'_e$.

The dimensions L_{cs} and L_s in Fig. 6(b) were adjusted roughly so that the support provided the least negative impact on the performance of the coaxial horn. A dielectric support with a total length of $L_s = \lambda_0$ and a cylindrical section with a length of $L_{cs} = \lambda_0/4$ resulted in reflection coefficients that remained below -20 dB for the majority of the Ka-band. Therefore, those were the dimensions used herein.

Introducing the transition region was required due to a disparity between the radii in the cylindrical region and those of a standard commercial connector. Consequently, a region providing gradual adjustment in the radii was necessary to facilitate the connection of the coaxial horn with a commercial connector, preserving performance and ultimately transforming it into a functional prototype.

Initially, the transition region took the form of a $\lambda_0/4$-long section of coaxial waveguide, with inner and outer radii determined by the geometric mean between the radii of the cylindrical region and those of a commercial 2.4 mm connector [14]. Following this, a parametric analysis explored variations in the length of the transition region (L_t), as well as in its inner (r''_i) and outer (r''_e) radii.

In the parametric analysis of L_t, seven variations were explored within a $\pm 50\%$ range of the original value (2.678 mm for $\lambda_0 = 10.714$ mm). The parametric analysis of the transition region's radii involved five variations of r''_e and five variations of r''_i. The considered range ensured that the minimum value corresponded to the radii of a commercial 2.4 mm connector [14], while the maximum value aligned with the radii in the cylindrical region: $max\{r''_e\} = r'_e$ and $max\{r''_i\} = r'_i$ (refer to Fig. 1).

The effect of modifying the length of the transition region is observed in Fig. 8, which shows a frequency shift in the reflection coefficient, yet it consistently stays below -20 dB across the majority of the Ka-band.

A subset of the results for the parametric analysis of the transition region's radii is presented in Fig. 9. Generally, the smallest and largest values of r''_e resulted in higher reflection coefficients, while intermediary values exhibited lower reflection coefficients. Notably, smaller r''_e values

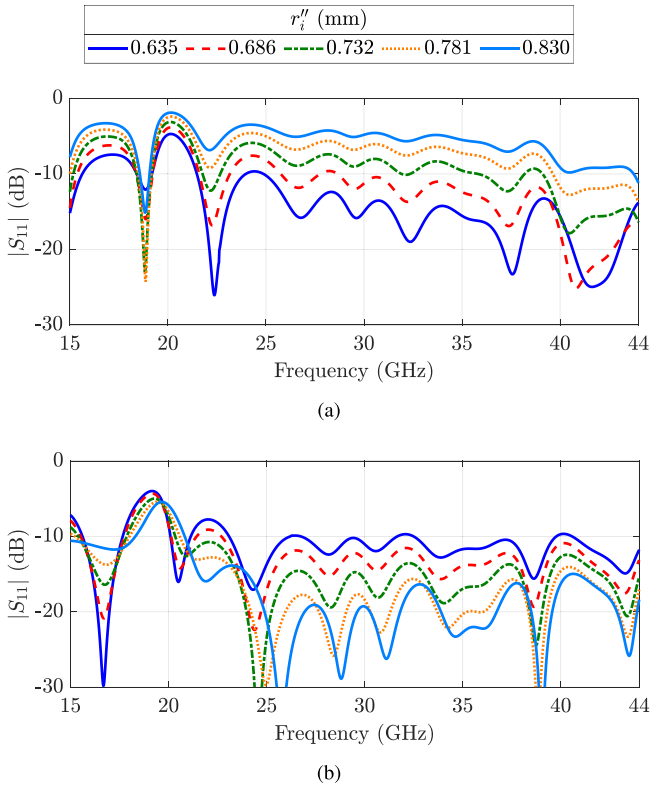

FIGURE 9. Reflection coefficients simulated via FEM for analyzed variations in the inner radius of the transition region (r_i''), considering an outer radius (r_e'') of (a) 1.27 mm, and (b) 1.91 mm.

correlated with lower reflection coefficients when r_i'' was also minimized (refer to Fig. 9(a)), whereas the opposite trend was observed for larger r_e'' (see Fig. 9(b)).

After examining the dielectric support and transition region through parametric analysis, one can deduce the presence of a considerable number of variables to manage and optimize. Optimization is necessary so that both added structures (support and transition) are dimensioned to have the least negative effect on the performance of the coaxial horn. Consequently, a heuristic optimization approach was employed. The optimizer used was the Genetic Algorithm (GA), built into HFSS Optimetrics, which allows the specification of the cost function and optimization goals based on any solution quantity that can be computed [22].

The optimization parameters, depicted in Fig. 1, were the transition region's length (L_s), the transition's inner and outer conductor's radii (r_i'' and r_e''), the length of the cylindrical section of the dielectric support (L_{cs}), and the total length of the support (L_s). The optimization goal introduced in the algorithm was $|S_{11}| \leq -20$ dB over the frequency range 26 GHz $\leq f \leq$ 40 GHz (Ka-band). Symmetry boundary conditions were used to reduce the computational time required by the FEM solver [22]. The parameters of the optimized design are listed in Table 1.

III. ANTENNA FABRICATION AND CHARACTERIZATION

Among the different additive manufacturing processes reported for metallic materials, L-PBF is the most consolidated variation for thin diameter struts (thinner than 1 mm) [24] or walls [25]. For that reason, in this research, we adopted L-PBF to produce metallic and polymeric dielectric components.

TABLE 1. Dimensions of the optimized coaxial horn antenna.

Parameter	Value (mm)	Parameter	Value (mm)
r_i	3.750	L_s	9.900
r_e	10.280	L_t	0.915
l_s	5.357	L_{cs}	2.000
w_s	1.243	r_i'	0.830
l_c	2.893	r_e'	1.908
w_c	0.911	r_i''	0.430
L	23.250	r_e''	1.353
r_c	10.708	L_c	10.714

An EOS M280 machine was used to fabricate the metallic components using a gas-atomized maraging steel powder feedstock. The powder presented a particle size between 16 and 45 μm, a constant layer thickness was of 30 μm and the scan strategy was 67° between layers. The chamber was filled with nitrogen gas to prevent oxidation. The laser power was 190 W, spot size of 100 μm. For these components, no post-heat treatments of machining were applied. The polymer components were fabricated in a Formiga P110 machine and using EOS polyamide 12 powders. Fully dense and with good-quality surface were obtained in the polymeric parts, therefore not post-processing were used.

The electromagnetic characterization was performed in an anechoic chamber provided by Albatross Projects GmbH (see Fig. 10 for reference), using a Keysight FieldFox Vector Network Analyzer model N995A. For the realized gain measurements, we used two identical Pasternack PE9850/2F-20 pyramidal horns [26]. We employed the two-antenna method [2, Sec. 17.4.1], supplemented by phase center corrections, to compute the gain of the standard horns. By comparison, we obtained the gain of the coaxial horn under test. The radiation efficiency was computed from the measurements of the co-polar radiation pattern and the maximum realized gain, according to the method in [2, Sec. 17.6].

The prototyped antenna is shown in Fig. 11, and Fig. 12(a) presents the absolute value of the measured S_{11} of the fabricated antenna compared with numerical results obtained via FEM from [22]. The fabricated antenna presents an absolute value of S_{11} below -10 dB over the measured range of 19 GHz to 44 GHz (VNA upper limit of measurement), but it presents some discrepancies with simulation results. In particular, the approximated reflection coefficient computation via (11) only accounted for the conical region and the coaxial aperture impedance mismatch, whereas the full-wave FEM solution considered the entire antenna geometry.

The simulated and measured results of the radiation patterns are presented in Fig. 12(b). Since the presented antenna exhibits minimal cross-polar response, only co-polar

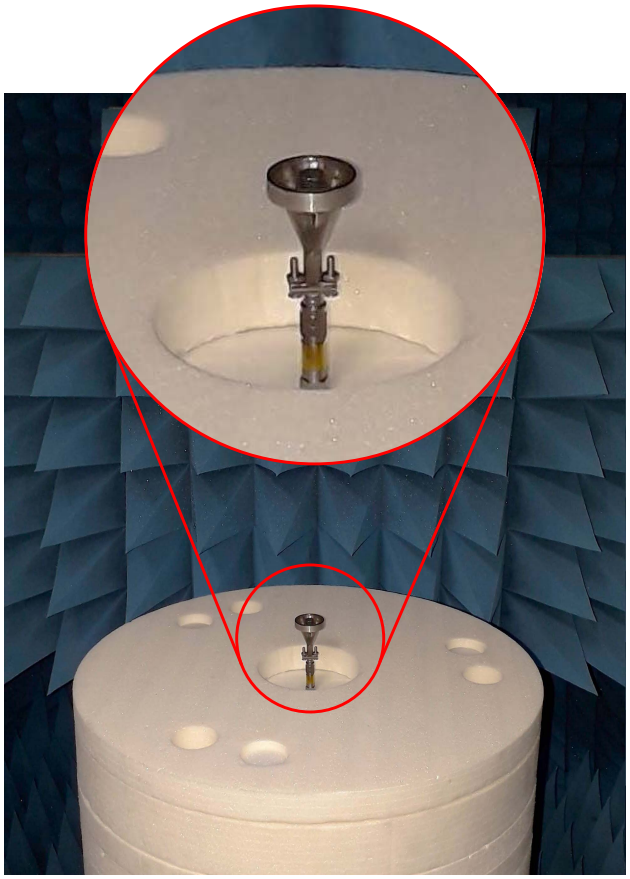

FIGURE 10. Photograph of the fabricated coaxial horn antenna installed in an anechoic chamber for measurements.

FIGURE 11. Photograph of the fabricated coaxial horn antenna placed next to a ruler with millimeter and centimeter graduations.

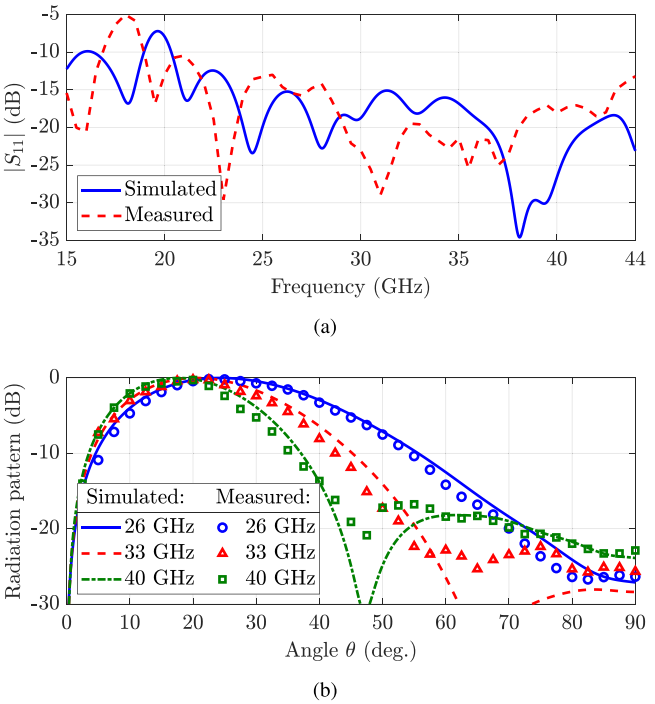

FIGURE 12. Simulated (via FEM) and measured results of the coaxial horn antenna. (a) Reflection coefficients $|S_{11}|$. (b) Normalized radiation patterns at 26 GHz, 33 GHz, and 40 GHz.

TABLE 2. Measured realized gain (G_{re}) and total antenna efficiency (e_0) of the fabricated prototype.

Frequency (GHz)	G_{re} (dBi)	e_0 (%)
26	8.37	84.37
33	10.27	89.83
40	11.53	88.25

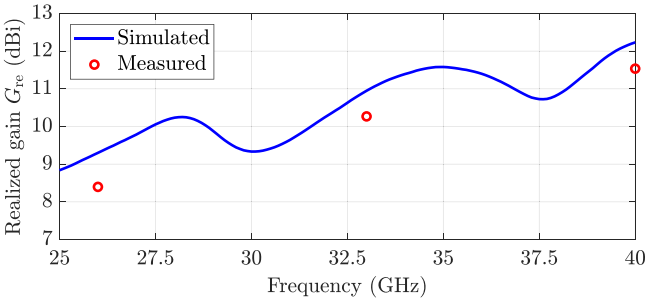

FIGURE 13. Simulated (via FEM) and measured results of the maximum realized gain of the horn antenna.

radiation results are presented. We can observe an increase in directivity for higher frequencies due to the aperture becoming electrically larger. The measurement results align well with the simulations at lower frequencies, but discrepancies become more noticeable at higher frequencies, particularly for $\theta > 60°$. The measured realized gain (G_{re}) and total antenna efficiency (e_0) of the fabricated prototype are presented in Table 2. The results indicate that the radiation efficiency is higher than 84.37%. Fig. 13 shows a comparison of the simulated and measured maximum realized gain of the horn antenna as a function of frequency. The observed radiation patterns exhibit highly consistent conical beams across the measured frequencies, with the maximum circularity deviation being less than 0.4 dB, observed at 40 GHz, as depicted in Fig. 14.

It should be noted that the calculation of the approximate reflection coefficient, as presented in (11), only accounts for

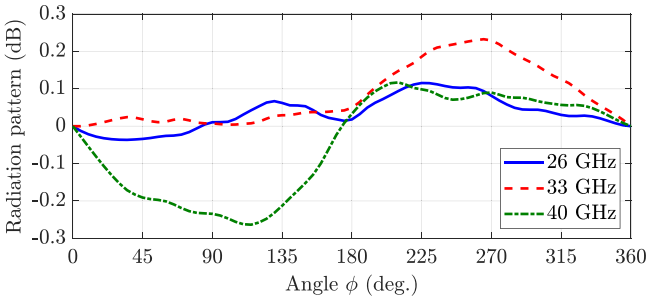

FIGURE 14. Measured normalized radiation patterns for 26 GHz, 33 GHz, and 40 GHz, observed at $\theta = 22.5^\circ$ as a function of the azimuth angle ϕ.

the conical region and the mismatch of impedance at the coaxial aperture. In contrast, the full-wave FEM solution considers the entire geometry of the antenna. This justifies the additional variations observed in the FEM solution of the reflection coefficient compared to the results shown in Fig. 3. The radiation patterns simulated by the simplified model (see Fig. 5) effectively capture the primary lobe radiation, highlighting the practical value of our approximate model in offering antenna design insights.

The disparities observed between the measurement and simulation results can be attributed to variations in the fabrication process, such as the different roughness values on the surfaces according to the building fabrication direction or crystallographic textures, i.e., roughness between 1-17 µm have been reported for the 316L processed by L-PBF [27]. Also, crystallographic textures, that are normally generated during additive manufactured metals [28], can affect the acoustic wave speeds [29]. The roughness was measured using a confocal microscope, resulting in an average roughness of $R_a = 3.27$ μm with a standard deviation of 0.21 μm. Manufacturing factors have a negligible effect on X-band antenna performance, while further studies are needed to accurately assess their impact on reflection coefficient and radiation patterns for Ka-band [30], [31].

In order to investigate some other features affecting the antenna's performance, several parametric analyses were conducted. We verify that the electric properties (ϵ_r and $\tan\delta$) of the dielectric supporting material do not lead to significant changes to the antenna reflection coefficient, besides the antenna efficiency being affected by the dielectric loss tangent.

The first two analyses involved varying the electrical properties (ϵ_r and $\tan\delta$) of the dielectric supporting material, as these properties are not well-documented for extremely high frequencies for the material adopted in the fabrication. In Fig. 15(a), where variations in ϵ_r are examined, a slight frequency shift in the reflection coefficient can be observed. However, even if the deviation becomes more pronounced above 37.5 GHz, they cannot fully explain the observed differences in the measurements shown in Fig. 12(a). Similarly, as shown in Fig. 15(b), variations of the dielectric loss tangent do not lead to significant changes in the reflection coefficient.

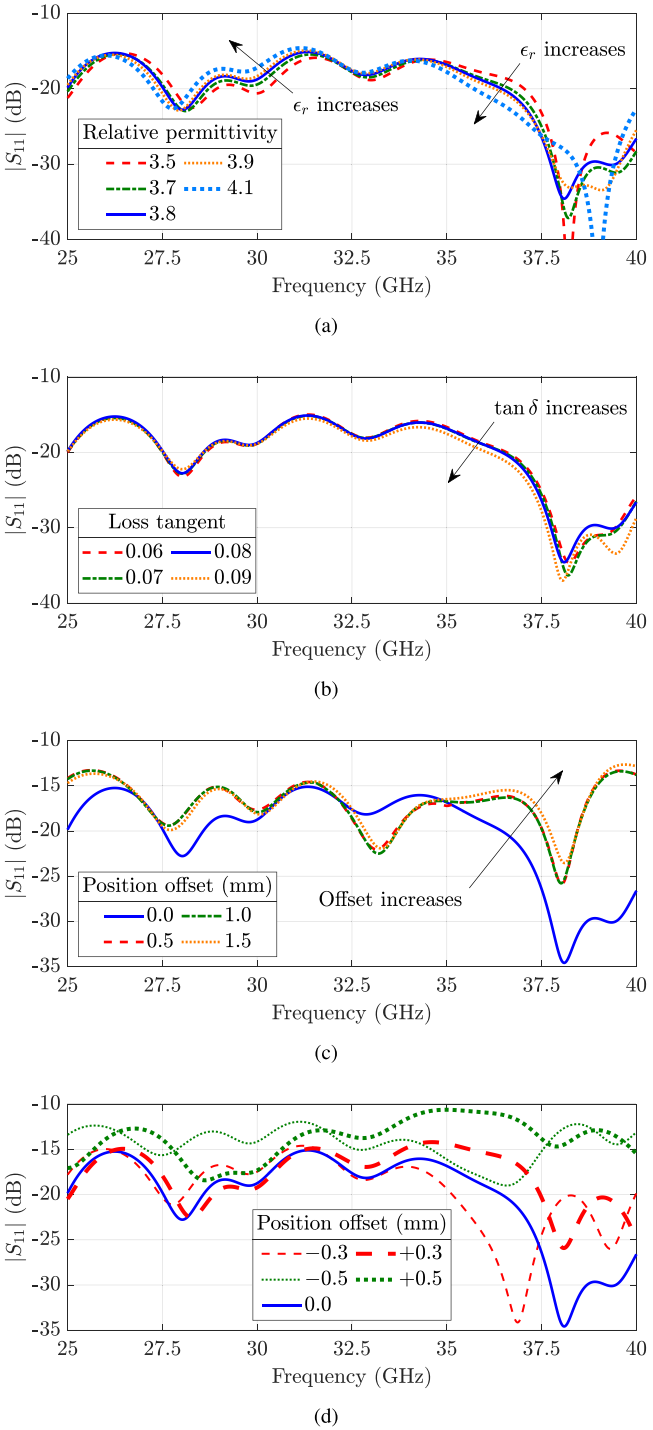

FIGURE 15. Parametric analyses for the reflection coefficient obtained via FEM. (a) Dielectric's relative permittivity (ϵ_r) (b) Dielectric's loss tangent ($\tan\delta$) (c) Dielectric support position offset. (d) Inner conductor position offset.

In contrast, during the assembly of the coaxial horn, it is possible that the dielectric support may not be perfectly aligned with the cylindrical region. To investigate this issue, a parametric analysis was conducted to examine the impact of offsetting the support position along the cylindrical region. Only offsets towards the conical region

TABLE 3. Performance comparison of the proposed antenna with other conical-beam antenna designs for mm-Wave applications.

Ref.	Center frequency (GHz)	10-dB impedance bandwidth (%)	Peak realized gain (dBi)	Dimensions (λ^3)
[6]	32.5	43.9	9.2	5.60 × 5.60 × 5.70
[11]	35.75	60.70	11.40	2.38 × 2.38 × 1.88
[32]	44.15	22.9	6.0	0.82 × 0.82 × 0.02
[33]	28.3	11.6	8.51	4.53 × 4.53 × 0.47
[34]	26.00	11.40	11.60	5.48 × 5.48 × 0.78
This work	31.50	79.36	11.53	2.61 × 2.61 × 3.66

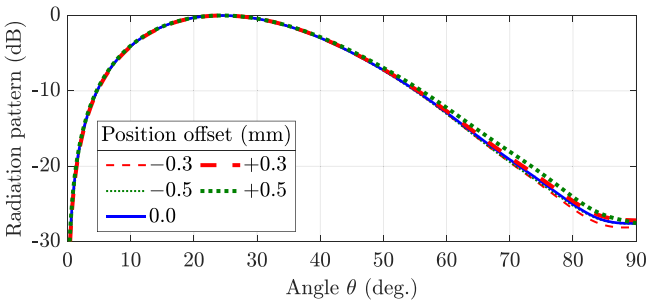

(a)

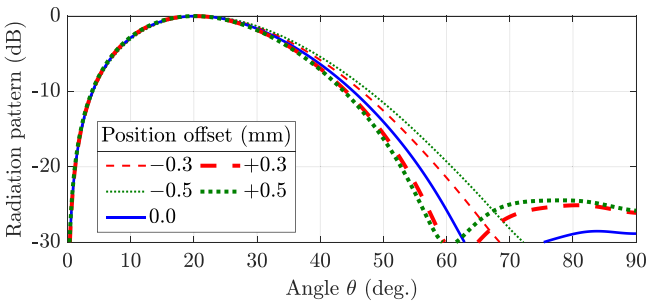

(b)

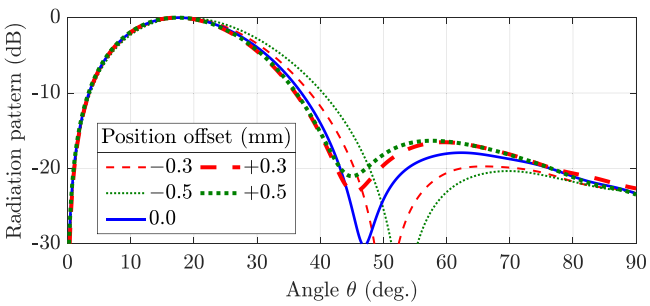

(c)

FIGURE 16. Normalized radiation patterns for variation in the inner conductor position obtained via FEM. (a) 26 GHz. (b) 33 GHz. (c) 40 GHz.

were considered since deviations in the opposite direction towards the connector are limited due to the presence of the transition region (see Fig. 1). The results shown in Fig. 15(c) demonstrate a significant influence of the offset on the reflection coefficient. However, the observed disparities are not influenced by the magnitude of the offset.

The assembly process can also affect the positioning of the inner conductor, which in turn impacts both the reflection coefficient and radiation pattern by altering the aperture geometry. To investigate this, we analyzed deviations in the inner conductor's position, considering positive offsets towards the aperture and negative offsets in the opposite direction. Fig. 15(d) shows the reflection coefficient for each analyzed offset, revealing significant performance changes even for offsets that are a fraction of the wavelength. Additionally, we examined the impact of the inner conductor's position on the radiation pattern. Fig. 16(a) shows that the inner conductor's position has minimal effect on the radiation pattern at 26 GHz. However, as the frequency increases, the observable impact on the radiation pattern intensifies. This is particularly evident at 40 GHz (see Fig. 16(c)), which may help explain the observed discrepancies in measurements in Fig. 12(b).

Table 3 presents a comparison of the coaxial horn antenna presented here with other recently reported conical-bean antennas from the works in [6], [11], [32], [33], [34]. The proposed antenna has the broadest impedance bandwidth in relation to other antennas with conical radiation patterns. Additionally, the peak realized gain is competitive, being merely 0.07 dB lower than that of the antenna reported in [34], despite our antenna having a smaller cross-sectional aperture.

For reference regarding the aperture efficiency ϵ_{ap}, the coaxial horn operating with the TEM mode considered in [12] exhibits $\epsilon_{ap} = 27.92\%$, while the TM_{01}-mode circular horn in [11] has $\epsilon_{ap} = 27.48\%$. The current coaxial horn achieves $\epsilon_{ap} = 35.86\%$. Compared to the coaxial design in [12], the major factor contributing to the improvements is the utilization of a ratio $r_e/r_i \approx 2.7$ in our design, whereas in the earlier work, the coaxial aperture had $r_e/r_i \approx 2$. These computations utilized the measured gains at the central operating frequency of each scenario, employing the definitions in [2, eq. (2-100) and eq. (2-112)].

IV. CONCLUSION

In this paper, we present the details of the design, fabrication, and characterization of a Ka-band coaxial horn antenna with a specialized dielectric supporting structure and a transition to a 2.4 mm connector using metal and polymer AM techniques. The prototyped antenna exhibits a measured −10-dB impedance bandwidth of above 79.36% (19–44 GHz), with a maximum measured realized gain of 11.53 dBi at 40 GHz. Moreover, the antenna demonstrates a maximum measured

radiation efficiency of 89.83% at 33 GHz, showcasing the potential of AM for fabricating specialized antennas for mm-wave applications. The conducted sensitivity analysis emphasizes the importance of precision and accuracy during fabrication to ensure the desired impedance matching and radiation characteristics are maintained. Work is in progress to further enhance the current model, particularly focusing on exploring the impact of surface roughness and crystallographic textures resulting from the AM process on the radiation efficiency of the antenna. Refining measurement techniques for roughness evaluation and integrating these imperfections into representative FEM solvers are being evaluated.

REFERENCES

[1] W. Stutzman and G. Thiele, *Antenna Theory and Design*, 3rd ed. Hoboken, NJ, USA: Wiley, 2012.

[2] C. A. Balanis, *Antenna Theory: Analysis and Design*, 4th ed. Hoboken, NJ, USA: Wiley, 2016.

[3] S. Liao, P. Chen, and Q. Xue, "Ka-band omnidirectional high gain stacked dual bicone antenna," *IEEE Trans. Antennas Propag.*, vol. 64, no. 1, pp. 294–299, Jan. 2016.

[4] J. L. McDonald and D. S. Filipovic, "A monocone-bicone collinear array," *IEEE Trans. Antennas Propag.*, vol. 58, no. 12, pp. 3905–3912, Dec. 2010.

[5] P. Sanchez-Olivares, J. L. Masa-Campos, E. Garcia-Marin, and D. Escalona-Moreno, "High-gain conical-beam Traveling-wave array antenna based on a slotted circular waveguide at *ku*-band," *IEEE Trans. Antennas Propag.*, vol. 68, no. 8, pp. 6435–6440, Aug. 2020.

[6] Z.-Y. Zhang, K. W. Leung, and K. Lu, "Wideband high-gain omnidirectional biconical antenna for Millimeter-wave applications," *IEEE Trans. Antennas Propag.*, vol. 71, no. 1, pp. 58–66, 2023.

[7] J. Ha, M. A. Al-Tarifi, and D. S. Filipović, "Design of wideband combined annular slot-monopole antenna," *IEEE Trans. Antennas Propag.*, vol. 64, no. 9, pp. 4138–4143, Sep. 2016.

[8] M. Zoghi, F. Hodjatkashani, and M. E. Lajevardi, "An ultra-wideband ridged biconical multibeam antenna," *IEEE Access*, vol. 11, pp. 58037–58045, 2023.

[9] R. Penchel, S. Zang, J. Bergmann, and F. Moreira, "GO shaping of omnidirectional dual-reflector antennas with arbitrary main-beam direction in elevation plane by connecting conic sections," *Int. J. Antennas Propag.*, vol. 2018, pp. 1–9, Mar. 2018.

[10] R. A. Penchel, S. R. Zang, J. R. Bergmann, and F. J. S. Moreira, "Design of wideband omnidirectional dual-reflector antennas in millimeter waves," *IEEE Antennas Wireless Propag. Lett.*, vol. 18, pp. 906–910, 2019.

[11] L. Wu, C. Wang, S. Peng, and Y. Guo, "3-D printed wideband millimeter-wave horn antenna with conical radiation pattern," *IEEE Antennas Wireless Propag. Lett.*, vol. 19, pp. 453–456, 2020.

[12] S. R. Zang and J. R. Bergmann, "Analysis of omnidirectional dual-reflector antenna and feeding horn using method of moments," *IEEE Trans. Antennas Propag.*, vol. 62, no. 3, pp. 1534–1538, Mar. 2014.

[13] E. Simionato, S. R. Zang, I. Aldaya, J. A. de Oliveira, G. S. Rosa, and R. A. Penchel, "Novel coaxial transition for shaped coaxial horn antennas operating at millimeter wave frequencies," in *Proc. IEEE Int. Symp. Antennas Propag. USNC-URSI Radio Sci. Meeting (AP-S/URSI)*, 2022, pp. 551–552.

[14] "FMCN1679 2.4 mm connector Datasheet," Data Sheet FMCN1679, Fairview Microw., Lewisville, TX, USA, 2020. Accessed: Dec. 5, 2023. [Online]. Available: https://www.fairviewmicrowave.com/images/productPDF/FMCN1679.pdf

[15] F. E. Gardiol, *Open-Ended Waveguides: Principles and Applications*, vol. 63. London, U.K.: Academic, 1985, pp. 139–187.

[16] S. Silver, *Microwave Antenna Theory and Design*. New York, NY, USA: McGrawHill, 1949.

[17] Z. Shen, J. Wang, and K. S. Lee, "Open-ended coaxial waveguide for conical-beam radiation," *IEEE Trans. Antennas Propag.*, vol. 60, no. 5, pp. 2518–2521, 2012.

[18] N. Marcuvitz, *Waveguide Handbook*. New York, NY, USA: McGrawHill, 1951.

[19] A. D. Olver, P. J. Clarricoats, A. A. Kishk, and L. Shafai, *Microwave Horns and Feeds* (Electromagnetic Waves). London, U.K.: IET, 1994. [Online]. Available: https://digital-library.theiet.org/content/books/ew/pbew039e

[20] C. Cockrell and P. Pathak, "Diffraction theory techniques applied to aperture antennas on finite circular and square ground planes," *IEEE Trans. Antennas Propag.*, vol. 22, no. 3, pp. 443–448, 1974.

[21] D. M. Pozar, *Microwave Engineering*, 4th ed. Hoboken, NJ, USA: Wiley, 2012.

[22] *Ansys HFSS 2023*, Ansys Inc., Canonsburg, PA, USA, 2023.

[23] "Product information: PA2200." EOS GmbH. Accessed: Jul. 3, 2023. [Online]. Available: https://www.epmi-impression-3d.com/pdf/EOS_PA12.pdf

[24] I. Maskery et al., "Mechanical properties of ti-6Al-4V selectively laser melted parts with body-centred-cubic lattices of varying cell size," *Exp. Mech.*, vol. 55, pp. 1261–1272, Sep. 2015.

[25] D. K. Pattanayak et al., "Bioactive Ti metal analogous to human cancellous bone: Fabrication by selective laser melting and chemical treatments," *Acta Biomaterialia*, vol. 7, pp. 1398–1406, Mar. 2011.

[26] (Pasternack Enterprises Inc., Irvine, CA, USA). *Pasternack PE9850/2F-20 Pyramidal Horns; Revision 1.2*. Nov. 2020. [Online]. Available: https://www.pasternack.com/images/ProductPDF/PE9850B-2F-20.pdf

[27] J. Liu et al., "Laser powder bed fusion of 316L stainless steel: Effect of laser polishing on the surface morphology and corrosion behavior," *Micromachines*, vol. 14, no. 4, p. 850, Apr. 2023.

[28] R. Santamaria et al., "Crystallographic texture and substructural phenomena in 316 stainless steel printed by selective laser melting," *Materials*, vol. 16, p. 4289, Jun. 2023.

[29] B. Lan et al., "Direct volumetric measurement of crystallographic texture using acoustic waves," *Acta Materialia*, vol. 159, pp. 384–394, Oct. 2018.

[30] R. A. Penchel et al., "Performance evaluation of a novel monofilar helical antenna with tapered cross-section wire fabricated via metal additive manufacturing," *AEU Int. J. Electron. Commun.*, vol. 175, Feb. 2024, Art. no. 155085.

[31] T. Whittaker, S. Zhang, A. Powell, C. J. Stevens, J. Y. C. Vardaxoglou, and W. Whittow, "3D printing materials and techniques for antennas and metamaterials: A survey of the latest advances," *IEEE Antennas Propag. Mag.*, vol. 65, no. 3, pp. 10–20, Jun. 2023.

[32] K. Fan, Z.-C. Hao, Q. Yuan, J. Hu, G. Q. Luo, and W. Hong, "Wideband horizontally polarized omnidirectional antenna with a conical beam for millimeter-wave applications," *IEEE Trans. Antennas Propag.*, vol. 66, no. 9, pp. 4437–4448, Sep. 2018.

[33] D. A. Pham, M. Lee, and S. Lim, "High-gain conical-beam planar antenna for Millimeter-wave drone applications," *IEEE Trans. Antennas Propag.*, vol. 69, no. 10, pp. 6959–6964, Oct. 2021.

[34] B. Feng, J. Lai, L. Li, C.-Y.-D. Sim, L. Deng, and X. Ding, "A dual-polarized shared-aperture antenna with conical radiation patterns and high gain for 5G millimeter-wave ceiling communications," *IEEE Trans. Antennas Propag.*, vol. 71, no. 3, pp. 2278–2289, Mar. 2023.

ELÍGIA SIMIONATO (Student Member, IEEE) received the B.Sc. degree in electronics and telecommunications engineering from the School of Engineering of São João da Boa Vista, São Paulo State University, São João da Boa Vista, Brazil. She is currently pursuing the M.Sc. degree with the Center for Advanced and Sustainable Technologies, where she is a Researcher. Her research interests include modeling and optimizing millimeter-wave devices and antennas.

IVAN ALDAYA (Member, IEEE) received the degree in telecommunications engineering from the Universidad Pública de Navarra and the Ph.D. degree in information and communications technologies from the Instituto Tecnológico y de Estudios Superiores de Monterrey, during which he carried out research internships with the Università di Bologna and the École Nationale Supérieure des Telecommunications. After the Ph.D., he was a Postdoctoral Researcher first with the Department of Optical Communications, Instituto Tecnológico y de Estudios Superiores de Monterrey and then with the Gleb Wataghin Institute of Physics, University of Campinas. He is currently an Assistant Professor with the Universidade Estadual de São Paulo and is part of the Center for Advanced and Sustainable Technologies Research Group. His main research areas are optical communications (including radio over fiber systems and digital coherent systems) and the application of artificial intelligence to optimize integrated photonic devices and antennas.

JOSÉ A. DE OLIVEIRA received the bachelor's degree in Business Administration from Ceuclar, the first master's degree in production engineering from Sao Paulo State University (UNESP), the second master's degree in environmental engineering from the Federal University of São Carlos (UFSCar), and the Ph.D. degree in production engineering from the University of São Paulo. He is a Professor with UNESP. He is a Researcher with the Group Center for Advanced and Sustainable Technologies. He has interest in the themes related to product life cycle engineering.

ANDRE L. JARDINI received the degree in mechanical engineering, and the master's and Doctoral degrees in mechanical engineering from the State University of Campinas in 1994, 1997, and 2001, respectively. He was a postdoctoral fellow with the Technology Center/UFRGS in 2001, with the Faculty of Chemical Engineering/UNICAMP in 2002, and with the Center for Rapid and Sustainable Product Development, the Polytechnic Institute of Leiria, Portugal, in 2004, working in the area of additive manufacturing for the development of technology, materials, and products. He is currently a Senior Researcher with the National Institute of Science and Technology in Biofabrication. He has 16 book chapters and two books published. He is the inventor of 12 patents, with participation in the development of several technological products, processes or innovative techniques. He works in the area of additive manufacturing, laser processing, development of new materials and technologies, and biomanufacturing. He received six Unicamp Inventor Awards.

JULIAN AVILA received the degree in mechanical engineer in 2008, the M.Sc. degree in materials engineering in 2011, and the Ph.D. degree in mechanical engineering in 2016. He has been working as an Associate Professor with São Paulo State University, Brazil, since 2017. In addition, he worked as a Postdoctoral Fellow with São Paulo University from 2016 to 2017. He is interested in the mechanical and microstructural characterization of materials submitted to different processing conditions. He has experience in additive manufacturing of metallic alloys, mainly related to the aerospace industry. The São Paulo Research Foundation has financed some of his research projects, the latest focused on studying Inconel alloys 625 and 718 AM parts processed by Directed Energy Deposition. Other projects in collaboration with AM involve maraging steel and aluminum alloys. He has extensive involvement in welding and joining; friction stir welding of aluminum, magnesium alloys, and high strength low alloy steels. He is a Serra Hunter Fellow and a CNPq Fellow.

GUILHERME S. DA ROSA (Senior Member, IEEE) received the B.S. degree in electrical engineering from the Federal University of Santa Maria, Santa Maria, Brazil, in 2011, and the M.S. and Ph.D. degrees in electrical engineering from the Pontifical Catholic University of Rio de Janeiro, Rio de Janeiro, Brazil, in 2013 and 2017, respectively, where he was a Professor with the Department of Electrical Engineering and Center for Telecommunications Studies from 2018 to 2024. In 2024, he joined São Paulo State University, São João da Boa Vista, Brazil, as a Professor with the School of Engineering. His current research interests include pseudo-analytical techniques for wave propagation modeling in complex media. He was a recipient of the Young Scientist Award from the URSI Commission B International Symposium on Electromagnetic Theory in 2019, and the Young Scientist Award from the General Assembly and Scientific Symposium of the International Union of Radio Science in 2017.

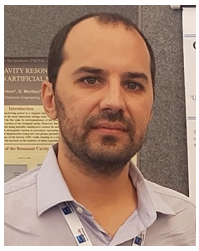

RAFAEL A. PENCHEL (Member, IEEE) received the B.Sc. degree in telecommunications engineering from FUMEC University, Belo Horizonte, Brazil, in 2006, the M.Sc. degree in electrical engineering from the Federal University of Minas Gerais in 2009, and the Ph.D. degree in electrical engineering from the Pontifical Catholic University of Rio de Janeiro in 2014. In 2015, he became a Postdoctoral Fellow with the National Institute of Telecommunications. Since 2017, he has been a Professor with the Department of Electronic and Telecommunications Engineering, São Paulo State University and also a part of the Center for Advanced and Sustainable Technologies Research Group. He has experience in electromagnetic theory with emphasis on microwave theory and antennas. His fields of research interest are passive devices and antennas for microwave and millimeter-wave frequency, mainly helical antennas, microstrip patch antennas, horn and reflector antennas; beamforming networks; and 3-D-printed antennas with complex geometries via plastic and metal additive manufacturing.